





High-performance infrared photodetectors based on InAs/InAsSb/AlAsSb superlattice for 3.5 μm cutoff wavelength spectra

JUNKAI JIANG,¹  GUOWEI WANG,^{1,2,3,5} DONGHAI WU,^{1,2,3} 
YINGQIANG XU,^{1,2,3} FARAN CHANG,¹ WENGUANG ZHOU,¹ NONG
LI,¹ DONGWEI JIANG,^{1,2,3} HONGYUE HAO,^{1,2,3} SUNING CUI,¹
WEIQIANG CHEN,¹ XUEYUE XU,¹ HAIQIAO NI,^{1,2,3} YING DING,⁴ AND
ZHI-CHUAN NIU^{1,2,3,*}

¹State Key Laboratory for Superlattices and Microstructures, Institute of Semiconductors, Chinese Academy of Sciences, Beijing 100083, China

²College of Materials Science and Opto-Electronic Technology, University of Chinese Academy of Sciences, Beijing 101408, China

³Center of Materials Science and Optoelectronics Engineering, College of Materials Science and Opto-Electronic Technology, University of Chinese Academy of Sciences, Beijing 100049, China

⁴James Watt School of Engineering, University of Glasgow, Glasgow, G12 8LT, UK

⁵wangguowei@semi.ac.cn

*zcnui@semi.ac.cn

Abstract: High-performance infrared p-i-n photodetectors based on InAs/InAsSb/AlAsSb superlattices on GaSb substrate have been demonstrated at 300K. These photodetectors exhibit 50% and 100% cut-off wavelength of $\sim 3.2 \mu\text{m}$ and $\sim 3.5 \mu\text{m}$, respectively. Under -130 mV bias voltage, the device exhibits a peak responsivity of 0.56 A/W, corresponding to a quantum efficiency (QE) of 28%. The dark current density at 0 mV and -130 mV bias voltage are $8.17 \times 10^{-2} \text{ A/cm}^2$ and $5.02 \times 10^{-1} \text{ A/cm}^2$, respectively. The device exhibits a saturated dark current shot noise limited specific detectivity (D^*) of $3.43 \times 10^9 \text{ cm}\cdot\text{Hz}^{1/2}/\text{W}$ (at a peak responsivity of $2.5 \mu\text{m}$) under -130 mV of applied bias.

© 2022 Optica Publishing Group under the terms of the [Optica Open Access Publishing Agreement](#)

1. Introduction

There is growing interest in 1.8-3.5 μm spectrum range infrared detectors, which are widely used in blood glucose monitoring [1] as well as H_2O , CH_4 , and CO_2 gas monitoring. In the past decade, infrared photodetectors based on InAs/GaSb type-II superlattices (T2SLs) have been great progress and are considered a potential alternative to other technologies. Recently, InAs/InAsSb (Gallium-free) strain balanced T2SL is a type of adjustable bandgap, broad-band III-V infrared detector material that is an alternative to InAs/GaSb T2SLs. Without defect recombination centers resulting from Ga atoms, InAs/InAsSb strain balanced T2SLs have a longer minority carrier lifetime [2–4] than that of traditional InAs/GaSb T2SLs.

Ga-free T2SLs infrared detection covers the spectrum range from 4.2 to 17 μm . As much attention paid to Ga-free T2SLs, a lot of work has been done about the main factor that influences the cut-off wavelength of this material system. Tuning the InAs and InAsSb layers thickness and Sb component in the InAsSb layer, the Ga-free T2SL cutoff wavelength moves from mid-wavelength to very long wavelength infrared spectrum [5]. Ga-free T2SL detectors for mid- [6], long [7], and very long [8] wavelength infrared wave-bands have been demonstrated. The InAs bandgap is $\sim 3 \mu\text{m}$ and InAsSb alloy has smaller bandgaps. Infrared detection at shorter wavelengths is not enough to rely solely on SLs of these two materials. Short-wavelength infrared detectors are fabricated based on Ga-free T2SLs by inserting AlAsSb layers [9]. Phosphorus (P)

element [10,11] joined in Ga-free T2SL has been studied in order to shift the cut-off wavelength to 1.6~3.5 μm .

In this paper, we design InAs/InAsSb/AlAsSb superlattice (SLs) structures, inserting AlAsSb layers into the InAsSb layer, to expand the cut-off wavelength from 2.1 μm [9] to 3.5 μm for multiple applications such as CH₄, H₂O, and CO₂ gas monitoring. The proposed superlattice structure is a type of M-structure SL [12] with GaSb replaced by InAsSb and AlSb replaced by AlAsSb. InAs/InAsSb/AlAsSb superlattices are grown in strain-balanced manner on GaSb substrate. Based on this, we fabricate p-i-n InAs/InAsSb/AlAsSb SLs infrared devices and present the optical and electrical properties of such devices.

To achieve high performance of p-i-n photodetectors, there are two challenges in the design of SL structures in the absorption region. The first challenge lies in absorption region materials that have a high electron effective mass and theoretically maintain a high absorption coefficient. The second challenge is good strain balance for superlattice with InAs, InAsSb and AlAsSb layers to keep high material quality. Defects due to poor strain balance have the potential to form surface leakage channels that increase dark current in the device. In order to address the first challenge, the wide band gap AlAsSb layer is inserted into the InAsSb layer. The wide band gap AlAsSb layer can block the interaction between electrons in the two adjacent InAs wells, which will reduce the tunneling probability and increase the electron effective mass. The large electron effective mass is one of the advantages of SL detectors over other materials. The insertion of the AlAsSb layer makes this advantage even more prominent. The Sb composition in both of the AlAsSb and InAsSb layers was chosen to be ~0.5 to achieve a good strain balance while reducing the thickness of the InAs, InAsSb and AlAsSb layers within one superlattice period. It is demonstrated that the reduction of the thickness of each material layer causes the decay of the carrier's localization and improves the spatial overlap of the electron wavefunction in the InAs quantum wells and the hole wavefunction in the InAsSb quantum wells, resulting in a larger absorption coefficient. However, reduction of layer thickness leads to nonuniformity in the interface among each layer and results in difficulty in epitaxy. With regard to this, 10/2/2/2 monolayers (MLs) of InAs/InAs_{0.5}Sb_{0.5}/AlAs_{0.5}Sb_{0.5}/InAs_{0.5}Sb_{0.5} per period were chosen to achieve a cut-off wavelength of around 3.5 μm . The molecular beam epitaxy (MBE) growth of the InAs/InAsSb/AlAsSb SLs in principle involves turning on and off the Sb, In and Al shutters as compared to the use of five shutters in the InAs/GaSb/AlSb SL. Besides, the growth of the InAs/GaSb/AlSb SL is actually more complex due to strain-balancing interfaces required to achieve high material quality.

Figure 1 shows the schematic diagram of the device design and the alignment of the conduction and valence band. The p-i-n device architecture consists of a thin *p*-type top contact, an *n*-type absorption region and an *n*-type bottom contact. Since top incidence was carried out in the single unit device testing, the top contact was designed to be thin to reduce the absorption in the contact region and improve the QE of the device. As demonstrated in Fig. 1(b), the M-structure SL, with colored region indicating the prohibited band of each material, consists of three members in one periodic sequence: InAs/InAsSb/AlAsSb/ InAsSb. At 300 K, the bandgap energy of InAs, AlAs_{0.5}Sb_{0.5} and InAs_{0.5}Sb_{0.5} are 354, 2131 and 114 meV, respectively. In comparison to the InAs/InAsSb superlattice, the AlAsSb layer lowers the valence band level. The barrier structure suitable for InAs/InAsSb/AlAsSb SLs is difficult to select. Also, this SLs are suitable for PBN devices but not nBn because of the lower bias dependence of the former.

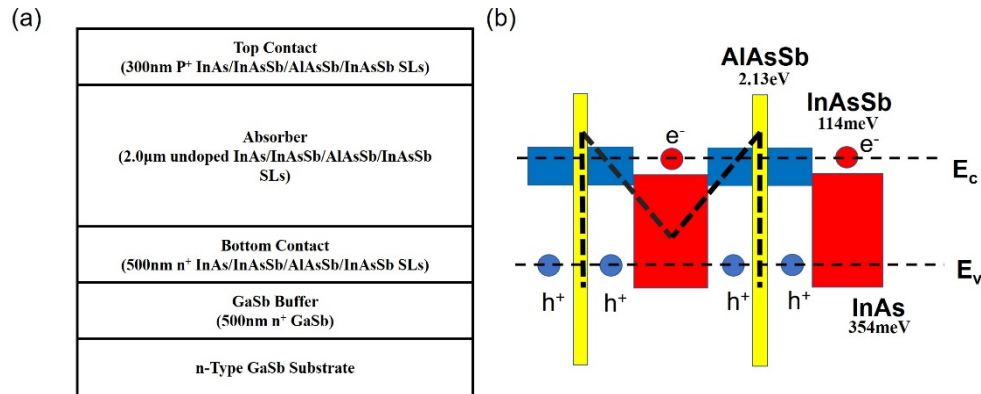


Fig. 1. (a) The schematic diagram of the InAs/InAsSb/AlAsSb SLs p-i-n infrared photodetector device structure. (b) The band alignment of the InAs/InAsSb/AlAsSb SLs for the absorption region and barrier. Colored rectangles represent the forbidden band gap of the semiconductors. At 300 K, the bandgap energy of InAs, AlAsSb and InAsSb are 354, 2131 and 114 meV, respectively.

2. Experiments

Epitaxy growth of InAs/InAs_{1-x}Sb_x/AlAs_{1-y}Sb_y/InAs_{1-x}Sb_x SLs was carried out on Tellurium (Te) doped *n*-type GaSb (001) substrates by Veeco Gen II Molecular Beam Epitaxy system equipped with group III SUMO cells and group V valved crackers using As₂ and Sb₂. The epitaxial growth of the photodetector was started with a 100 nm thick GaSb buffer layer to smooth out the surface, then a 500 nm thick *n*-doped (10¹⁸ cm⁻³) GaSb buffer layer, followed by a 500 nm thick *n*-doped (10¹⁸ cm⁻³) bottom contact layer, a 2.0 μm thick un-intentionally doped absorption layer, and a 300 nm thick *p*-doped top contact layer. The top and bottom contacts share the same superlattice design as the absorption layer. Silicon (Si) and beryllium (Be) were used for *n*-type and *p*-type dopants in the bottom and top contacts, respectively. Tellurium (Te) was used for the 500nm GaSb buffer layer.

After the epitaxial growth, the material quality was characterized using atomic force microscopy (AFM) and high-resolution X-ray diffraction (HR-XRD). Figure 2 shows the structural characterization results of the as-grown material. The AFM image exhibits morphology of the sample showing clear atomic steps in absence of dislocation and a small RMS of 2.37 Å over 20 μm × 20 μm area. The satellite peaks in the HR-XRD scan show the overall periods of the absorption region in good agreement with the theoretical designs. And the simulation results demonstrate that a 10.2/2.1/1.9/2.1 ML InAs/InAsSb/AlAsSb/InAsSb superlattice has been fitted and calculated. The lattice mismatch between the absorption layer and the GaSb substrate is less than ~500 ppm. The HRXRD also shows the slightly splitted-up satellite peak. It is an evidence of Sb segregation or composition variation throughout the device structure. The sample was subsequently processed into mesa-isolated single element photodetectors with diameters ranging from 100 μm to 500 μm using a standard lithography technique. Ti/Au was deposited for both top and bottom Ohmic contacts. No additional passivation and anti-reflection coating were applied to the devices. The sample was wire-bonded onto a 68-pin leadless chip carrier.

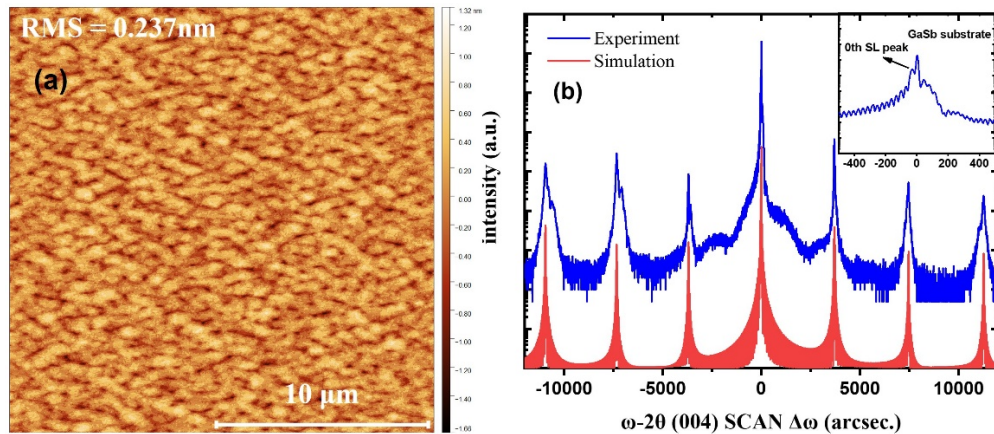


Fig. 2. (a) The atomic force microscopy image over $20\ \mu\text{m} \times 20\ \mu\text{m}$ surface area of the pin device with an RMS roughness value of $2.37\ \text{\AA}$. (b) HR-XRD and simulation curve of p-i-n device. The inset shows that the GaSb substrate and the InAs/InAsSb/AlAsSb SLs 0^{th} diffraction peak.

3. Results and discussion

Figure 3(a) shows the electrical performance of a p-i-n device, measured over a temperature range of 90 K to 300 K. The diameter of test device mesa was $500\ \mu\text{m}$ and the bias voltage was applied to the *p*-doped top-contact region. At 300 K, the dark current density at 0 mV and -130 mV bias voltage were $8.17 \times 10^{-2}\ \text{A/cm}^2$ and $5.02 \times 10^{-1}\ \text{A/cm}^2$, respectively. The -130 mV bias voltage was the saturated bias for QE and responsivity in the optical test. At 150 K, the dark current density at 0 mV and -130 mV bias voltage were $4.99 \times 10^{-6}\ \text{A/cm}^2$ and $3.20 \times 10^{-5}\ \text{A/cm}^2$, respectively. The dark current at 0 V is not the measurement minimum value. The reason is that the photodetector saw the room emissions during the electrical test without a cold shield. At 300 K, the differential resistance area product (RA) was $5.70\ \Omega\text{cm}^2$ at -130 mV. Figure 3(b) shows the Arrhenius plot of dark current density vs the inverse of temperature under the applied bias of -130 mV. The calculated activation energy at temperatures ranging from 180 K to 300 K is 348 meV, close to the theoretically designed bandgap energy ($E_g = 354\ \text{meV}$) of the absorption region and $3.5\ \mu\text{m}$ cut-off wavelength from the response spectra. From 120 K to 180 K, activation energy is slightly less than half of the bandgap energy, representing generation-recombination (G-R) current as the dominating dark current. The calculated activation energy at temperatures ranging from 70 K to 120 K is 73 meV, less than a quarter of the bandgap energy. It should be demonstrated that the surface states result in the band inversion of the surface and form a channel of surface leakage current, without any barrier as broad-band gap materials blocking it. Under 120 K, surface leakage current turns into the dominant part of dark current.

The optical characterization was carried out at 300 K, by using a Bruker VERTEX 70 Fourier transform infrared (FTIR) spectrometer for measuring spectrum response, with a 500°C blackbody source for QE and responsivity. The optical characterization results of photodetectors, without any anti-reflection (AR) coating, are shown in Fig. 4. The devices exhibit 50% and 100% cut-off wavelengths of $\sim 3.2\ \mu\text{m}$ and $\sim 3.5\ \mu\text{m}$ at 300 K, respectively. Under -130 mV bias voltage, the device exhibits a peak responsivity of $0.56\ \text{A/W}$, corresponding to a QE of 28%. As shown in Fig. 4(c), the QE of the photodetector reaches 12% and continues rising to 28% with bias voltage increasing to -130 mV at $2.5\ \mu\text{m}$. Saturated QE and responsivity reach 28% and $0.56\ \text{A/W}$, more than double those at zero bias voltage, indicating the existence of a threshold voltage for the photodetector. Working at room temperature is a harsh condition for infrared photodetector

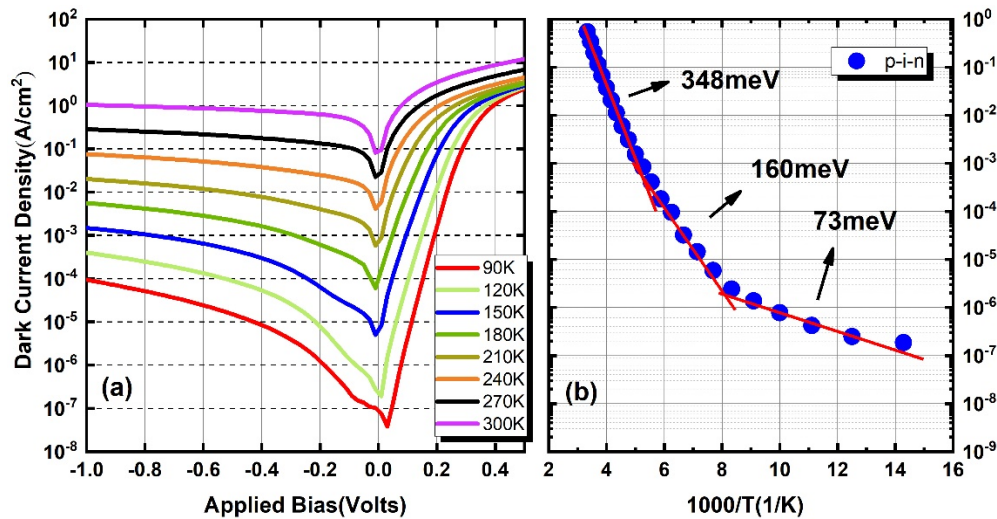


Fig. 3. (a) Dark current density vs applied bias voltage characteristic of the photodetectors as temperatures rising from 90 K to 300 K. (b) Arrhenius plot of the dark current of the photodetectors under -130 mV applied bias. Red lines stand for linear fit for blue point in the figure, demonstrating that 348 meV, 160 meV and 73 meV activation energy represents for the point from 180 K to 300 K, 120 K to 180 K and 70 K to 120 K, respectively.

that increases Auger recombination and decreases minority carrier diffusion length, which has been researched by Wu et al [13]. It is generally believed that high saturated bias voltage exists in barrier infrared detectors (BIRDs) resulting from valence band offset (VBO) between the absorption region and barrier region with different materials. In this letter, the QE of the photodetector at zero bias voltage is around 12% not close to ~28% saturated QE [14]. The main factor is poor mobility of minority carriers due to high temperature. It is demonstrated that the QE decreases at shorter-wavelengths, caused by partial absorption of short-wavelength light in the top SWIR *p*-contact without any contribution to photo current in the device [15]. Thinner top contacts can be a solution for it.

After the electrical and optical characterization, the device's specific detectivity was calculated. Figure 5(a) indicates that the device exhibits a saturated dark current shot noise limited specific detectivity (D^*) of $3.43 \times 10^9 \text{ cm}\cdot\text{Hz}^{1/2}/\text{W}$ (at a peak responsivity of $2.5 \mu\text{m}$) under -130 mV of applied bias. Corresponding with QE and responsivity curves, the specific detectivity of the device reaches a saturated value as applied bias rises to -130 mV and remains almost unchanged with applied bias adding to -150 mV at 300 K, demonstrated in Fig. 5 inset. With zero bias applied, the specific detectivity of the device is $2.28 \times 10^9 \text{ cm}\cdot\text{Hz}^{1/2}/\text{W}$, not much less than that of saturated value, which indicates the capacity of working in the small even zero bias disregarding the low QE. It is demonstrated that the background-limited infrared performance (BLIP) detectivity for an ideal photodetector is $6.93 \times 10^{11} \text{ cm}\cdot\text{Hz}^{1/2}/\text{W}$, on the condition that the QE is 100% with a $3.5 \mu\text{m}$ cut-off wavelength for an immersed 300 K background with a 2π field of view (FOV). Figure 5(b) shows the specific detectivity vs operating temperature at $2.5 \mu\text{m}$ and BLIP specific detectivity slightly beyond that of 150 K. The specific detectivity at $2.5 \mu\text{m}$ was calculated from the responsivity obtained by the black body test, which was more accurate. The detectivity at $2.5 \mu\text{m}$ was also the peak detectivity. In addition, the specific detectivity remains a high level for a broad region between short-wave and mid-wave infrared spectrum, making the photodetector a potential choice for multiple applications.

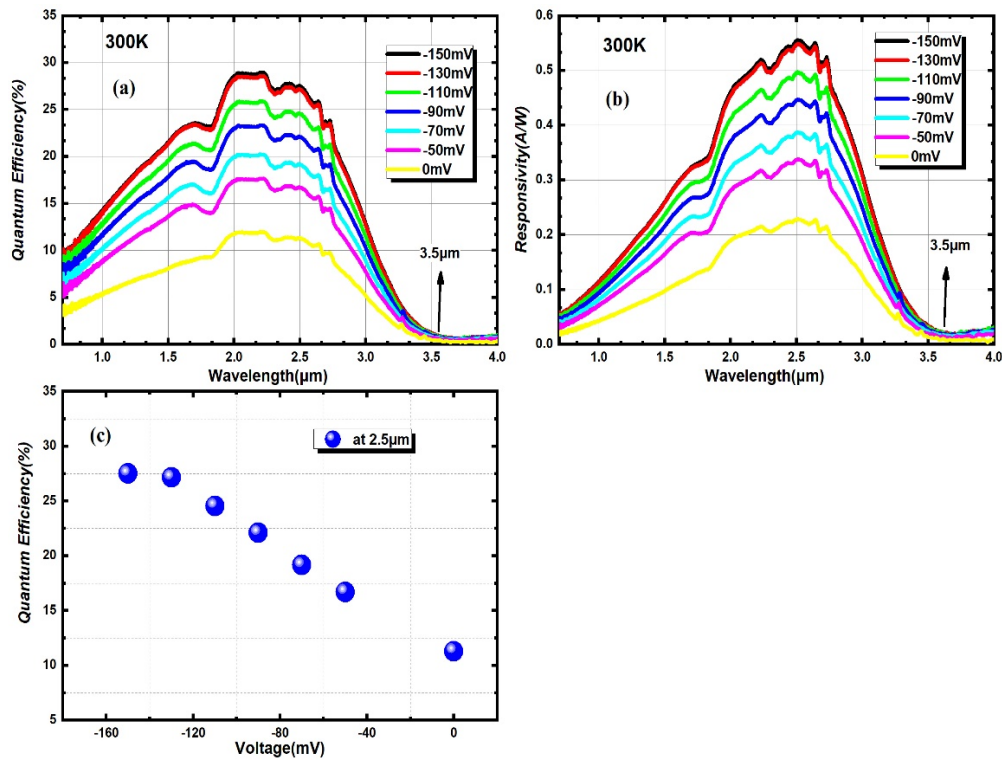


Fig. 4. (a) Saturated quantum efficiency spectrum and (b) saturated responsivity of the p-i-n photodetectors with a 2 μm-thick absorption region at -130 mV applied bias voltage in front illumination configuration without any anti-reflection coating. (c) Saturated quantum efficiency at 2.5 μm from 0 mV to -150 mV.

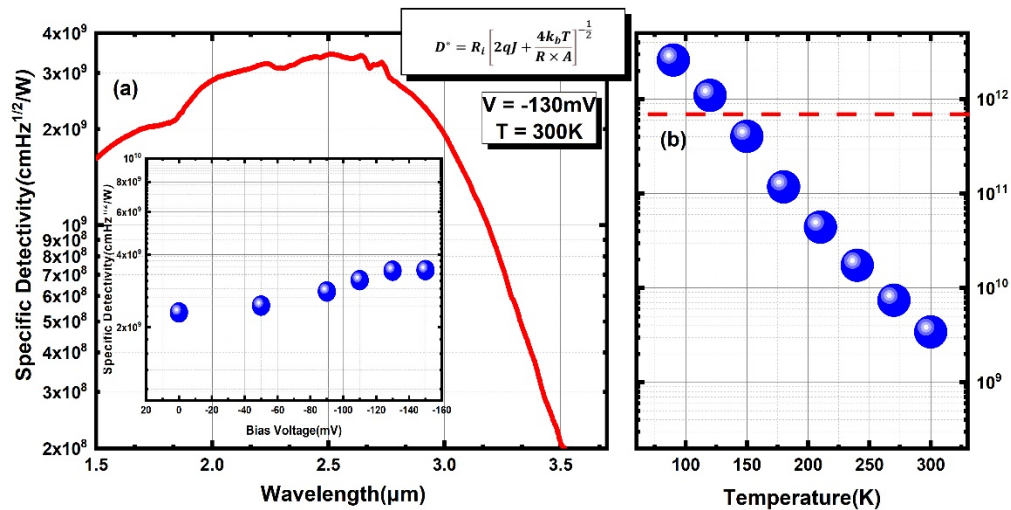


Fig. 5. (a) Specific detectivity (D^*) spectrum of the p-i-n photodetector at 300 K at a -130 mV applied bias voltage in the front illumination configuration without any anti-reflection coating. The inset shows the specific detectivity vs applied bias voltage. (b) Specific detectivity vs temperature and the red line represents the BLIP detectivity for an ideal photodetector with 2π field of view with 300 K background.

4. Conclusion

In conclusion, we report the design, growth, and characterization of a 3.5 μm cut-off wavelength pin photodetector based on InAs/InAsSb/AlAsSb SLs on GaSb substrate. The AFM images show the atomic steps with RMS roughness value of 2.37 \AA . Satellite peaks in the HR-XRD scan show the overall periods of the absorption region in good agreement with the theoretical designs. The lattice mismatch between the absorption layer and the GaSb substrate is less than ~ 500 ppm. At 300 K, the dark current density was $8.17 \times 10^{-2} \text{ A/cm}^2$ at a 0 mV bias voltage and $5.02 \times 10^{-1} \text{ A/cm}^2$ at a -130 mV bias voltage. The sample exhibits 50% and 100% cutoff wavelengths of $\sim 3.2 \mu\text{m}$ and $\sim 3.5 \mu\text{m}$ at 300 K, respectively. Under -130 mV bias voltage, the device exhibits a peak responsivity of 0.56 A/W, corresponding to a QE of 28%. At 300 K, the device exhibits a saturated dark current shot noise limited specific detectivity (D^*) of $3.43 \times 10^9 \text{ cm}\cdot\text{Hz}^{1/2}/\text{W}$ (at a peak responsivity of 2.5 μm) under -130 mV of applied bias. With zero bias applied, the specific detectivity of the device is $2.28 \times 10^9 \text{ cm}\cdot\text{Hz}^{1/2}/\text{W}$, not much less than that of saturated value, which indicates the capacity of working in the small even zero bias without considering the low QE.

Funding. Chinese Aeronautical Establishment (20182436004); Major Program of the National Natural Science Foundation of China (61790581); Key Technologies Research and Development Program (2018YFA0209104, 2019YFA0705203).

Disclosures. The authors declare no conflicts of interest.

Data availability. No data were generated or analyzed in the presented research.

References

1. K. Maruo, T. Oota, M. Tsurugi, T. Nakagawa, H. Arimoto, M. Tamura, Y. Ozaki, and Y. Yamada, "New Methodology to Obtain a Calibration Model for Noninvasive Near-Infrared Blood Glucose Monitoring," *Appl. Spectrosc.* **60**(4), 441–449 (2006).
2. E. H. Steenbergen, B. C. Connelly, G. D. Metcalfe, H. Shen, M. Wraback, D. Lubyshev, Y. Qiu, J. M. Fastenau, A. W. K. Liu, S. Elhamri, O. O. Cellek, and Y. H. Zhang, "Significantly improved minority carrier lifetime observed in a long-wavelength infrared III-V type-II superlattice comprised of InAs/InAsSb," *Appl. Phys. Lett.* **99**(25), 251110 (2011).
3. B. V. Olson, E. A. Shaner, J. K. Kim, J. F. Klem, S. D. Hawkins, L. M. Murray, J. P. Prineas, M. E. Flatté, and T. F. Boggess, "Time-resolved optical measurements of minority carrier recombination in a mid-wave infrared InAsSb alloy and InAs/InAsSb superlattice," *Appl. Phys. Lett.* **101**(9), 092109 (2012).
4. B. C. Connelly, G. D. Metcalfe, H. Shen, and M. Wraback, "Direct minority carrier lifetime measurements and recombination mechanisms in long-wave infrared type II superlattices using time-resolved photoluminescence," *Appl. Phys. Lett.* **97**(25), 251117 (2010).
5. D. Z. Ting, A. Soibel, A. Khoshakhlagh, S. A. Keo, S. B. Rafol, A. M. Fisher, C. J. Hill, E. M. Luong, B. J. Pepper, S. D. Gunapala, G. F. Fulop, C. M. Hanson, and B. F. Andresen, "The emergence of InAs/InAsSb type-II strained layer superlattice barrier infrared detectors," in *Infrared Technology and Applications XLV* (2019).
6. G. Deng, D. Chen, S. Yang, C. Yang, J. Yuan, W. Yang, and Y. Zhang, "High operating temperature pBn barrier mid-wavelength infrared photodetectors and focal plane array based on InAs/InAsSb strained layer superlattices," *Opt. Express* **28**(12), 17611–17619 (2020).
7. A. Haddadi, G. Chen, R. Chevallier, A. M. Hoang, and M. Razeghi, "InAs/InAs_{1-x}Sb_x type-II superlattices for high performance long wavelength infrared detection," *Appl. Phys. Lett.* **105**(12), 121104 (2014).
8. A. M. Hoang, G. Chen, R. Chevallier, A. Haddadi, and M. Razeghi, "High performance photodiodes based on InAs/InAsSb type-II superlattices for very long wavelength infrared detection," *Appl. Phys. Lett.* **104**(25), 251105 (2014).
9. A. Haddadi, X. V. Suo, S. Adhikary, P. Dianat, R. Chevallier, A. M. Hoang, and M. Razeghi, "High-performance short-wavelength infrared photodetectors based on type-II InAs/InAs_{1-x}Sb_x/AlAs_{1-x}Sb_x superlattices," *Appl. Phys. Lett.* **107**(14), 141104 (2015).
10. M. Ahmetoglu, I. A. Andreev, E. V. Kunitsyna, K. D. Moiseev, M. P. Mikhailova, and Y. P. Yakovlev, "Electrical and optical characteristics of the InAs/InAs_{0.7}Sb_{0.1}P_{0.2} single heterojunction photodiodes for the spectral range 1.6–3.5 μm ," *Infrared Phys. Technol.* **55**(1), 15–18 (2012).
11. M. A. Afrailov, "Photoelectrical characteristics of the InAsSbP based uncooled photodiodes for the spectral range 1.6–3.5 μm ," *Infrared Phys. Technol.* **53**(1), 29–32 (2010).
12. B.-M. Nguyen, M. Razeghi, V. Nathan, and Gail J. Brown, "Type-II M structure photodiodes: an alternative material design for mid-wave to long wavelength infrared regimes," *Proc. SPIE* **6479**, 64790S (2007).
13. D. Wu, J. Li, A. Dehzangi, and M. Razeghi, "Mid-wavelength infrared high operating temperature pBn photodetectors based on type-II InAs/InAsSb superlattice," *AIP Adv.* **10**(2), 025018 (2020).

14. B. F. Andresen, M. Razeghi, G. F. Fulop, E. K. Huang, B.-M. Nguyen, P. R. Norton, S. Abdollahi Pour, and P.-Y. Delaunay, "Type-II antimonide-based superlattices for the third generation infrared focal plane arrays," in *Infrared Technology and Applications XXXVI* (2010).
15. A. Haddadi, R. Chevallier, A. Dehzangi, and M. Razeghi, "Extended short-wavelength infrared nBn photodetectors based on type-II InAs/AlSb/GaSb superlattices with an AlAsSb/GaSb superlattice barrier," *Appl. Phys. Lett.* **110**(10), 101104 (2017).